



Shape optimization of annular transonic thrust nozzles via genetic algorithm and adjoint method

Younes Narimani ^{a,1}, Amir Joulaei ^{a,1}, Ahmad Shirvani ^{a,1}, Mahdi Nili-Ahmabadi ^{a,*}, Man Yeong Ha ^{b,*}

^a Isfahan University of Technology, Department of Mechanical Engineering, Isfahan, 84156-83111, Iran

^b School of Mechanical Engineering, Pusan National University, Busan, Republic of Korea

ARTICLE INFO

Keywords:
 Shape optimization
 Genetic algorithm
 Adjoint method
 Thrust force
 Annular nozzle
 Conical center body

ABSTRACT

In this research, the idea of combining the genetic algorithm and adjoint method was proposed to leverage the benefits of both approaches to improve the accuracy of thrust nozzle shape optimization. Although the genetic algorithm can search the entire design space to approach the global optimum, its computational cost increases considerably with the number of design variables. Meanwhile, the adjoint method is unaffected by the design variables, but it cannot achieve the global optimum directly and relies on the initial guess geometry. To address these challenges, a genetic algorithm was initially employed to approximate the global optimal geometry of a thrust nozzle with a conical center body parameterized by a Bezier curve. A MATLAB code integrated the geometry parameterization, genetic algorithm, and Fluent R2 2021 flow solver. The resulting geometry was then considered as the initial guess for the adjoint method, which accurately achieved the final optimal geometry with increased control points. The genetic algorithm aimed to maximize the thrust coefficient as the objective function, while the adjoint solver aimed to minimize the axial velocity variance at the nozzle outlet as the cost function. Three distinct constraints were incorporated in the optimization process, and the influence of the center body shape on the results was thoroughly examined to consider all possible geometries throughout the optimization procedure. The findings revealed that the conical center body effectively adjusted the flow angle at the exit, significantly affecting the thrust force. Both optimization steps reduced the average velocity and increased the average pressure at the nozzle exit, enhanced the mass flow rate, and finally increased the thrust force. The genetic algorithm and adjoint method contributed to 3 % and 0.6 % increases, respectively, in the thrust force, resulting in a thrust coefficient of 96.15 % for the final optimized nozzle.

Nomenclature

Symbol		
A_c	Base area of cone at nozzle exit plane (m^2)	u_j y-velocity (m. s^{-1})
A_e	Nozzle exit area (m^2)	V_e Axial velocity at nozzle outlet (m. s^{-1})
C_t	Thrust coefficient	W Flow field variables
F	Force (N)	β' Factor in $k-\omega$ SST model
F	Geometry variable in adjoint equations	β_2 Factor in $k-\omega$ SST model
F_x	Force applied to outer part of cone (N)	γ specific heat ratio

(continued on next column)

(continued)

I	Cost function in adjoint equations	γ_2	Factor in $k-\omega$ SST model
k	Turbulent kinetic energy ($\text{m}^2 \cdot \text{s}^{-2}$)	δ_{ij}	Kronecker delta
M	Mach number	λ	Thermal conductivity ($\text{W. K}^{-1} \cdot \text{m}^{-2}$)
\dot{m}	Mass flow rate	μ	Dynamic viscosity ($\text{kg. m}^{-1} \cdot \text{s}^{-1}$)
P	Static pressure (Pa)	μ_t	Eddy viscosity ($\text{kg. m}^{-1} \cdot \text{s}^{-1}$)
P_a	Ambient pressure (Pa)	ρ	Density (kg. m^{-3})
P_0	Stagnation pressure (Pa)	σ^2	Axial velocity variance (m. s^{-1}) ²

(continued on next page)

* Corresponding author.

** Corresponding author.

E-mail addresses: m.nili@iut.ac.ir (M. Nili-Ahmabadi), myha@pusan.ac.kr (M.Y. Ha).

¹ Co-First authors.

(continued)

P_e	Nozzle exit pressure (Pa)	$\sigma_{\omega,1}$, $\sigma_{\omega,2}$	Factor in $k-\omega$ SST model
P_{wall}	Static pressure on the cone (Pa)	τ_{ij}	Reynolds stress ($\text{kg} \cdot \text{m}^{-1} \cdot \text{s}^{-2}$)
S_i	Energy source term ($\text{W} \cdot \text{s}^{-1}$)	τ	Shear stress ($\text{kg} \cdot \text{m}^{-1} \cdot \text{s}^{-2}$)
S_{ij}	Mean rate of deformation (s^{-1})	ω	Turbulence frequency (s^{-1})
T	Temperature (K)	Abbreviation	
T	Thrust (N)	<i>CFD</i>	Computational Fluid Dynamics
T_0	Stagnation temperature (K)	GA	Genetic algorithm
R	Gas constant ($\text{J}/(\text{mol} \cdot \text{K})$)	SST	Shear-stress transport
R	Nozzle outlet radius (m)	RANS	Reynolds-averaged Navier-Stokes
u_i	x-velocity ($\text{m} \cdot \text{s}^{-1}$)		

1. Introduction

Thrust nozzles play a crucial role in propulsion systems, particularly in transonic and supersonic conditions. Achieving the optimal thrust efficiency under these conditions requires careful topology optimization of the nozzle. This optimization becomes even more complex when additional features such as thrust vectoring and thrust reversing are required, necessitating a high degree of geometric flexibility in the exhaust nozzle system [1]. Computational fluid dynamics (CFD)-based optimization techniques have gained momentum in recent decades [2–5]. Engineers can develop automated design approaches with several advantages by combining CFD simulations with optimization algorithms. Some advantages include simplification of the design process, fostering innovation in design solutions, and reducing the engineering workload and design time. These methods include the method of characteristics [6,7], alternate-direction method [8], alternating variable method [9], central composite design [10], evolutionary algorithm [11, 12], genetic algorithm (GA) [13], and adjoint method [13–15]. Among all these methods, the GA and adjoint methods are popular approaches applied to topology optimization problems owing to their advantages. The GA excels at efficiently exploring extensive design spaces and identifying global optimal solutions. In contrast, the adjoint method is advantageous since its computational cost is unaffected by any increase in design variables.

The classical methods of optimizing nozzle profiles were usually based on the method of characteristics and the calculus of variations [6]. In this method, modeling starts with an inviscid flow model; subsequently, a boundary layer correction is added to compensate for viscous effects. However, Rao [16] showed that the performance of the optimal nozzle obtained by the characteristic method can be approximated by a slight reduction in thrust force with an asymmetric term. The design of a convergent-divergent nozzle using the calculus of variations to achieve optimal thrust force is limited to nozzle lengths greater than a certain limit. For shorter lengths, providing a solution free of shock waves is impossible; this region is referred to as the invalid region. However, Rao et al. [17] developed a method for designing a divergent nozzle profile in the invalid region for chemical equilibrium and frozen chemistry conditions. Allman and Hoffman [18] proposed direct optimization methods to design nozzle profiles for maximizing the thrust force. The divergent nozzle profile was defined by a second-degree polynomial with constant initial expansion, and gas dynamic-flow modeling was performed using the equations of isentropic flow and assuming a perfect gas. Sternin [19] compared three design methods for nozzle profiles: the calculus of variations method with and without internal shocks, the truncated nozzle method with uniform characteristics, and the arcs circular conjugate method. Among these approaches, the first design method was the most efficient for viscous and inviscid flows.

In recent decades, a combination of CFD and optimization algorithms has gained considerable attention, owing to the advancements in numerical methods and computational power. Nili-Ahmabadi et al. [20] developed a hybrid optimization approach for curved diffusers that integrates a genetic algorithm, a CFD solver, and an inverse design

algorithm. They employed the genetic algorithm to optimize the wall pressure distribution and determined the optimal geometry through the inverse design process. Xing and Damodaran [21] used a logical nonuniform B-spline method to describe the geometric shape of a three-dimensional nozzle with an elliptical cross-section. The optimization performed on this geometric shape yielded better results than the traditional geometric shapes and third-degree splines. Both Navier–Stokes and Euler flow solvers were used to evaluate the performance of the optimized nozzle. Cai et al. [22] optimized a liquid rocket engine nozzle using a CFD code and three optimization algorithms, including second-order sequential quadratic programming, a GA, and an interdigitation strategy (combined hybrid algorithm), to achieve optimal thrust. The implementation of optimization algorithms resulted in an improvement of approximately 1.5 % in performance. Mon and Lee [23] combined characteristic-based techniques and optimization algorithms for reducing the length of a supersonic nozzle while preserving its exit area and validated their results by CFD analysis. Yumusak and Eyi [24] developed a reliable and efficient design tool for rocket nozzle design; in this design tool, a CFD code for solving axisymmetric reactive Euler equations was incorporated into an optimization code. A comparison between the baseline and optimized nozzles revealed an increase in thrust production by approximately 2%–4%. Yumusak [25] integrated a gradient-based optimization method with an axisymmetric reactive Navier–Stokes solver to optimize the thrust generated by a solid rocket motor nozzle with the constraint of constant propellant weight. A comparison of the initial and optimized nozzle showed an increase of 47.9 % in the thrust. Yu et al. [26] simultaneously maximized the thrust and static pressure recovery coefficient of a convergent–divergent nozzle profile. The proposed convergent–divergent nozzle profile consisted of three sections composed of fourth-degree polynomials. This multi-objective optimization resulted in a 27.4 % increase in thrust and a 63.4 % increase in the static pressure recovery coefficient. Kraiko et al. [13] parameterized the nozzle profile in the form of a Bezier curve and optimized the profile using the GA considering the thrust force as the objective function. They designed different geometries and optimized these geometries in three stages in which different angles and rotations of the flow in the nozzle throat were applied. The thrust force increased by a total of 1.7 % over the three stages.

Annular nozzles with center bodies outperform conventional bell nozzles by reducing the base losses [7] and offering enhanced performance owing to their capability to adjust the surrounding environment via modification of the outer jet boundary [7]. Davidenko et al. [27] worked on annular nozzles with center bodies and used second- and third-degree polynomials to fit the nozzle profile; they combined direct optimization methods with a two-dimensional reactive flow solver to achieve a nozzle profile with maximum thrust in the presence of a central body. The results showed that increasing the diameter of the cones of short nozzles improves the thrust force but does not greatly affect long nozzles. Kumar et al. [28] enhanced the performance of an aerospike nozzle under different conditions, optimizing the key design parameters on truncated and bleed-based models. CFD analysis was performed to examine flow behavior. The 40 % truncated bleed-based configuration generates 14.35 % higher thrust than the full-length nozzle, while simultaneously reducing the weight of the nozzle by approximately 29 %. Kartashev and Kartasheva [9] optimized annular nozzles with external expansion with polyphase working media to achieve the maximum thrust using direct methods based on the calculus of variations. This variational problem was transformed into a nonlinear programming problem. The optimal configurations of annular nozzles were designed under different conditions to prevent the deposition of particles from a condensed phase on the nozzle walls. Tillyaeva et al. [7] designed a spike nozzle using the method of characteristics that is similar to Rao's method and optimized this nozzle by using the GA. In applying the GA, they used the Navier–Stokes equations to solve the flow. The use of the GA increased the thrust force by 2.3 %.

In the past decade, the adjoint method has been widely used in

topology optimization problems, particularly in the field of aerodynamic design [29]. Jameson [30,31] was the first to apply the adjoint method to aerodynamic design problems in transonic flow regimes. He derived the formulations of this method for compressible, inviscid flow accompanied by shock waves using Euler equations, as well as for potential flow. The results demonstrated the applicability and usefulness of this method for airfoil design in transonic flow. Jameson [32] also introduced the adjoint method for three-dimensional Euler problems. Hassan Saeed et al. [33] enhanced the power coefficient of the Savonius turbine by 14.7 % through the utilization of the adjoint method. Iollo et al. [34] employed the continuous adjoint method for shape optimization in one-dimensional and two-dimensional flows. They obtained the adjoint equations and their boundary conditions for a convergent–divergent nozzle in quasi-one-dimensional flow and numerically solved these equations. Giles and Pierce [35] used Green's function method to analytically solve the adjoint equations for quasi-one-dimensional flow in a nozzle and analyzed the adjoint variables in the throat and shock wave regions of the nozzle. Cliff et al. [36] applied an inverse design using adjoint equations to a supersonic divergent nozzle with supersonic inflow. Soto et al. [37] used the adjoint method to optimize the geometries of the divergent sections of a simple convergent–divergent nozzle and an annular nozzle based on the thrust cost function. All points along the nozzle geometry were considered as design variables. The results indicated that the optimization method delivered a better performance for the simple convergent–divergent nozzle. Yerlikaya [38] optimized the geometry of the exhaust nozzle of an aircraft engine by the adjoint method under geometric constraints of fixed inlet and outlet areas and constant length. The objective function comprised the mass flow rate and the outlet Mach number, and appropriate weighting and combination were adopted to obtain a function suitable for this purpose. The optimization also took into account the aerodynamic constraint of constant total pressure. The results demonstrated that the most remarkable geometric changes occurred in the throat region. Ultimately, optimization yielded a 2 % increase in thrust.

The present study deals with the topology optimization of a convergent thrust nozzle with a conical center body. The methodology was based on a dual approach that combines a GA as a metaheuristic tool and an adjoint method as a gradient-based technique. In the optimization by metaheuristic methods, increasing the number of optimization iterations either enhances the value of the objective function or maintains it constant. In contrast, in the gradient-based methods, optimization eventually leads to a diminishing objective function value after a certain number of iterations because these methods can get trapped in the local optima and cannot escape them. Hence, excessive iterations in the optimization cycle can cause a shift away from the local optimum. The adjoint method is suitable for topology optimization when dealing with a large number of design variables and results in flexibility in the geometric changes, whereas the GA is appropriate for finding the global optimum when the number of design variables is limited. Therefore, a twofold strategy was considered. Initially, the GA was used within the search domain, and the geometric constraints were considered to obtain the approximate global optimal. Then, the final geometry obtained from the GA was refined using the adjoint method. In this work, the nozzle geometry was optimized in three configurations using the proposed hybrid method. These three configurations differed from each other in terms of the location of the conical section within the nozzle. The effects of the conical region on thrust and flow properties were examined.

2. Flow numerical solution

2.1. Governing equations

Two-dimensional axisymmetric Reynolds-averaged Navier–Stokes equations (RANS) equations, which describe the mass, momentum, and energy conservation (Eqs. (1)–(3)), were used to simulate the compressible flow throughout the thrust nozzle. The working fluid was

air, which was regarded as an ideal gas.

Continuity equation

$$\frac{\partial \rho}{\partial t} + \frac{\partial(\rho u_i)}{\partial x_i} = 0 \quad \text{Eq. 1}$$

Momentum equation

$$\frac{\partial(\rho u_i)}{\partial t} + \frac{\partial(\rho u_i u_j)}{\partial x_j} = -\frac{\partial p}{\partial x_i} - \frac{\partial}{\partial x_i} (\rho \bar{u}_i \bar{u}_j) + \frac{\partial}{\partial x_j} \left(\mu \frac{\partial u_i}{\partial x_j} \right) \quad \text{Eq. 2}$$

In this equation, τ_{ij} is a stress tensor and is defined as $\tau_{ij} = -\frac{1}{2} \rho \bar{u}_i \bar{u}_j = 2\mu_t S_{ij}$, where S_{ij} is the mean rate of the strain tensor.

Energy equation

$$\frac{\partial(\rho c_p T)}{\partial t} + \frac{\partial(\rho c_p u_i T)}{\partial x_j} = \frac{\partial}{\partial x_j} \left(\lambda \frac{\partial T}{\partial x_j} \right) - \tau_{ij} \frac{\partial u_i}{\partial x_j} \quad \text{Eq. 3}$$

The $k - \omega$ shear stress transport (SST) turbulence model developed by Menter et al. [39,40] was used to calculate the Reynolds stress term (Eqs. (4) and (5)) in the momentum equation.

k equation

$$\frac{\partial(\rho k)}{\partial t} + \frac{\partial(\rho k u_j)}{\partial x_j} = \frac{\partial}{\partial x} \left(\mu + \frac{\mu_t}{\sigma_k} \right) \frac{\partial k}{\partial x} + \left(\tau_{ij} S_{ij} - \frac{2}{3} \rho k \frac{\partial \rho u_i}{\partial x_j} \delta_{ij} \right) - \beta^* \rho k \omega \quad \text{Eq. 4}$$

ω equation

$$\frac{\partial(\rho \omega)}{\partial t} + \frac{\partial(\rho \omega u_j)}{\partial x_j} = \frac{\partial}{\partial x} \left(\mu + \frac{\mu_t}{\sigma_{\omega,1}} \right) \frac{\partial \omega}{\partial x} + \gamma_2 \left(2\rho S_{ij} S_{ij} - \frac{2}{3} \rho \omega \frac{\partial \rho u_i}{\partial x_j} \delta_{ij} \right) - \beta_2 \rho \omega^2 + 2 \frac{\rho}{\sigma_{\omega,2}} \frac{\partial k}{\partial x_k} \frac{\partial \omega}{\partial x_k} \quad \text{Eq. 5}$$

The constant coefficients $\sigma_{\omega,1}$ and μ_t were used together in a combination function, which is useful for both near-wall and far-field regions, and the other coefficients σ_k , β^* , $\sigma_{\omega,2}$, γ_2 , and β_2 are equal to 2.0, 0.009, 1.17, 0.44, and 0.083, respectively. Launder and Sandham [41] provide the concrete principles of $k-\omega$ (SST) model in which μ_t is set as shown in Eq. (6).

$$\mu_t = \frac{a_1 K}{\max(a_1 \omega, SF_2)}, \quad \text{Eq. 6}$$

where K stands for the turbulence kinetic energy; ω is the specific dissipation rate; the specific value for a_1 is 0.31; and F_2 is equal to 0 in the boundary layer and 1 in the free shear layer flow.

2.2. Computational domain and boundary conditions

The computational domain must be adequately extended downstream of the thrust nozzle exit to correctly simulate the high-velocity flow inside and outside the nozzle. Extending the domain ensures a comprehensive simulation of the exhaust jet shear layer. Insufficient dimensions of the computational domain can adversely affect numerical convergence and the accuracy of the obtained results. Conversely, an excessively large domain leads to increased computational costs. In this work, the length and height of the domain downstream of the nozzle exit were chosen to be 30 and 5 times the diameter of the nozzle exit, respectively [42]. To mitigate computational costs, two-dimensional axisymmetric conditions were considered for this problem, which is a prevalent approach in the literature for simulating thrust nozzles, as supported by prior studies [7,28,43–45].

The initial dimensions of the thrust nozzle were obtained by the preliminary design of a thrust nozzle, assuming an ideal isentropic gas flow and using gas dynamics equations. The purpose of the desired nozzle was to accelerate the subsonic flow with an input Mach number

of 0.57 to an output transonic flow with a Mach number of 1. The thrust nozzle conditions were considered according to the static cold test conditions. Thus, the stagnation temperature at the inlet was taken as the ambient temperature (300 K), and the static pressure at the outlet was the ambient pressure (92.3 kPa). Assuming the Mach number of the nozzle outlet as one, and considering ideal isentropic at the outlet, the stagnation pressure of the nozzle was calculated from the following equation, resulting in a value of 175 kPa.

$$P_0 = P \left(1 + \frac{\gamma - 1}{2} M^2 \right)^{\gamma / (\gamma - 1)} \quad \text{Eq. 7}$$

Therefore, by considering ideal isentropic Assuming a mass flow rate of 19.17 kg/s, the nozzle inlet and outlet areas were obtained from the following equation.

$$\frac{m\sqrt{RT_0/\gamma}}{AP_0} = \frac{M}{\left(1 + \frac{\gamma-1}{2} M^2 \right)^{(\gamma+1)/2(\gamma-1)}} \quad \text{Eq. 8}$$

The inlet cross section of the nozzle was assumed to be annular with an average diameter of 30 cm, and the outlet cross section was circular. The length of the initial nozzle was set as 80 cm. **Table 1** lists the input and output parameters in the preliminary design.

For the numerical solution, the stagnation pressure and temperature for the inlet, the static pressure (ambient pressure) for the outlet, and the axisymmetric line for the nozzle centerline were considered the boundary conditions. **Fig. 1** shows the computational domain and boundary conditions adopted in the numerical simulation. The values for these boundary conditions are listed in **Table 2**. Importantly, in the numerical simulation, the stagnation pressure of the inlet was derived by summing the calculated stagnation pressure from Eq. (7) and an estimated stagnation pressure loss across the nozzle.

2.3. Numerical method

Fluent 2022R2 software was used for conducting numerical simulations of fluid flow. The flow was assumed to be a steady-state and axisymmetric two-dimensional flow, considering both compressibility and viscosity. A pressure-based solver was used to solve the problem. The coupling between velocity and pressure was executed through a coupled algorithm, and an equation for pressure correction was obtained. The first-order upwind approach was applied to the turbulence equations, whereas the momentum and energy equations were treated using the second-order upwind approach. The pressure was interpolated by using a second-order method. A least-squares method centered around the cell was implemented to determine the gradients of essential quantities for computing the diffusion terms, velocity derivatives, and higher-order discretization. Convergence analysis was executed by ensuring that the residual of the continuity equation was less than 10^{-5} ; for the remaining equations, the residual was maintained below 10^{-6} .

2.4. Grid independency

Grid generation is one of the most important steps in numerical simulations. The use of an appropriate mesh leads to more accurate solutions and faster convergence of numerical simulations. However, if the mesh is insufficient, the residuals of the numerical solution may not

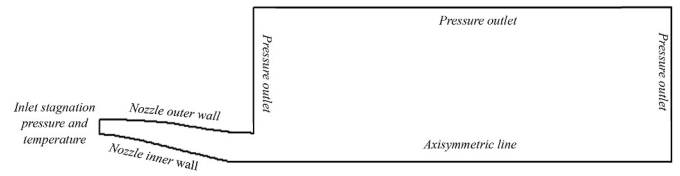


Fig. 1. Numerical domain and boundary conditions.

Table 2
Values of the boundary conditions for the numerical solution.

Boundary conditions	Value
Inlet stagnation pressure	175 kPa
Inlet stagnation temperature	300 K
Turbulence intensity	5 %
Outlet static pressure	92.3 kPa

decrease and may even diverge in some cases. The structured mesh used in this work is shown in **Fig. 2**. Seven structured meshes of different sizes were generated to investigate the effect of mesh size on the results. The coarsest and the finest mesh had 3800 and 139,000 cells, respectively. The thrust generated by the nozzle and mass flow rate were compared for these meshes. **Fig. 3(a)** and (b) illustrate the relationship between the number of cells and the corresponding thrust and mass flow rate. The slope of the thrust and mass flow rate decreased as the number of cells increased. Specifically, the thrust generated by the 39,000-cell mesh was only 0.36 % less than that of the 139,000-cell mesh. A similar trend is observed in **Fig. 3(b)** for changes in the mass flow rate. **Fig. 3(c)** shows a comparison of the velocity distributions at the nozzle exit using the 39,000-cell and 139,000-cell meshes; a good agreement is observed. Hence, the 39,000-cell mesh was used in this study.

2.5. Validation

The present numerical simulations were validated through comparison with numerical or experimental data from previous studies. The geometry, numerical domain, and boundary conditions were consistent with those employed in earlier studies, and the simulations were conducted using a mesh similar to that depicted in **Fig. 2**. In particular, our numerical results were compared with the outlet pressure and mass flow rate data obtained by Nair et al. [45] from the CFD analysis of truncated conical plug nozzles, and with the wall pressure distributions measured by Verma [46] in experiments for annular conical aerospike nozzles.

Table 3 presents a comparative analysis between the outcomes of the present simulation and those from the study conducted by Nair et al. [45]. The current simulation exhibits a 0.4 % deviation in mass flow rate and a 1.3 % deviation in exit pressure, indicating good agreement. **Fig. 4** compares the wall pressure distributions for the annular conical aerospike nozzle at two pressure ratios, derived from our simulation and Verma's experimental study [46], indicating a favorable agreement.

The close agreement between the current numerical results and the previous numerical and experimental data validates the computational methodology and numerical setup employed in the present work, lending confidence to the subsequent analysis and findings.

3. Topology optimization

3.1. Objective function

The objective function plays a crucial role in the optimization process since it connects the physical problem under optimization with the optimization methodology. Therefore, to measure the nozzle thrust as the desired objective function for optimization, a suitable control volume encompassing the entire propulsion system and nozzle (**Fig. 5**) was

Table 1
Preliminary design: input and output parameters.

Input parameters	Value	Output parameter	Value
Inlet Mach number	0.57	Inlet area	575.5 cm ²
Outlet Mach number	1.0	Outlet area	470 cm ²
Ambien pressure	92.3 kPa	Ideal mass flow rate	19.17 kg/s
Inlet stagnation temperature	300 K	Nozzle length	80 cm

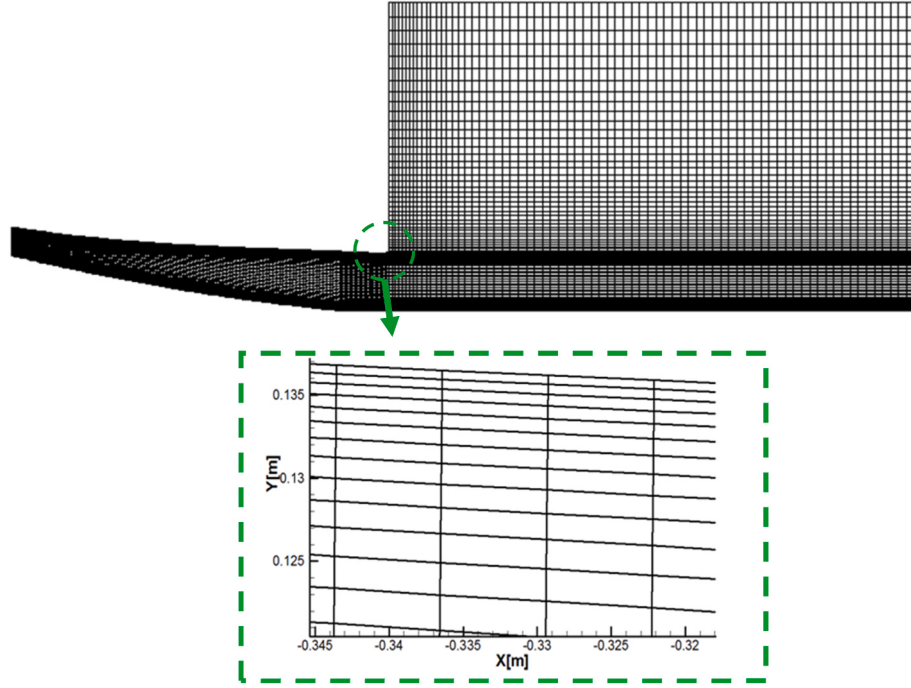


Fig. 2. Structured mesh for the numerical domain.

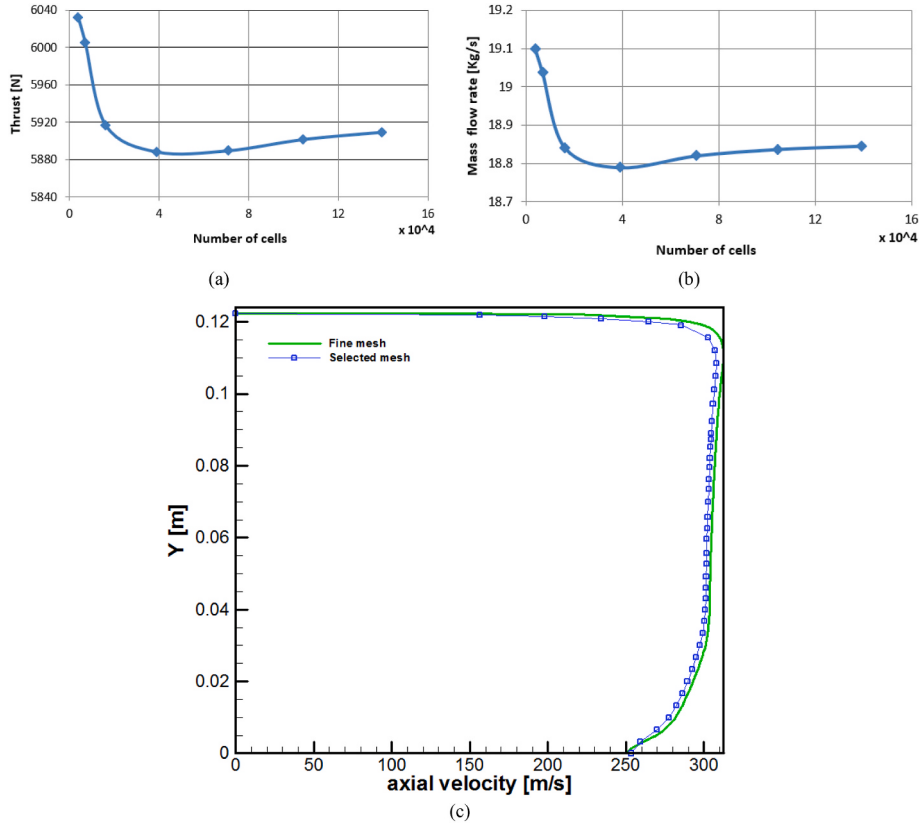


Fig. 3. (a) Thrust value and (b) mass flow rate for different number of grids, and (c) velocity distribution at the exit of nozzle for the selected and fine mesh.

considered. As indicated in Fig. 5, we ensured that the inlet boundary of the control volume was sufficiently distant from the engine inlet. Since the thrust force was calculated under stationary engine conditions, velocities on all boundaries except the nozzle exit were set to zero, indicating stationary air far from the engine inlet. In addition, the static

pressure on all boundaries was set to ambient pressure (P_a) except for the nozzle exit, which was set to P_e . It is important to note that if the conical part of the nozzle extends beyond the nozzle exit plane, the pressure exerted on the outer part of the cone is not equal to P_a , resulting in an x-force (F_x) being applied to it (Fig. 6).

Table 3

Comparison of values reported by Nair et al. [45] and current numerical results.

	Cells	Mass Flow Rate (kg/s)	Pressure at exit (Pa)
Nair et al. [45]	293,961	0.68317	68,403.62
Present study	84,651	0.67994	69,344.29
Error	–	–0.4 %	1.3 %

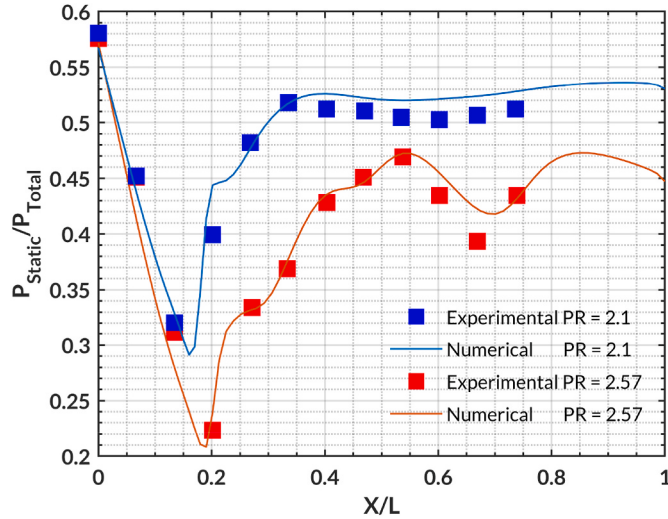


Fig. 4. Comparison of wall pressure distributions obtained from the current numerical simulations and experimental measurements by Verma [46] at two pressure ratios.

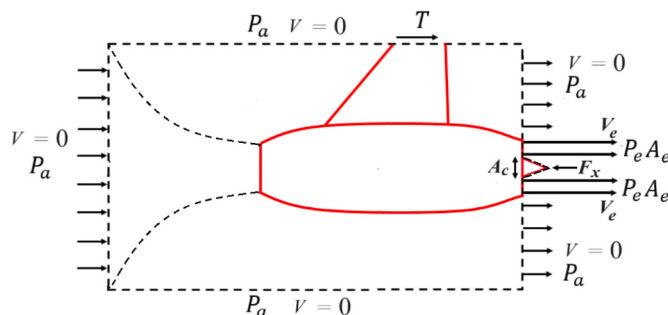


Fig. 5. Control volume of a propulsion system for calculating thrust force.

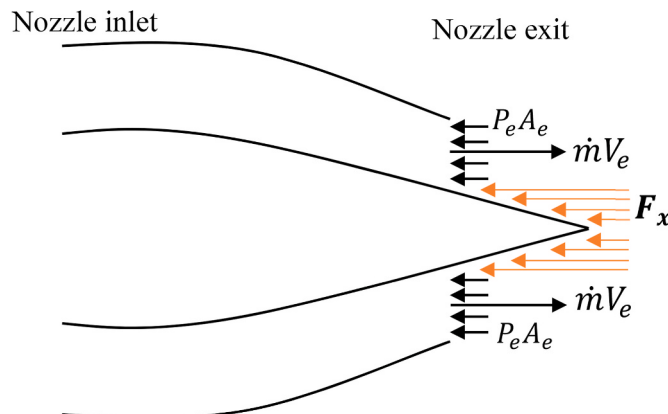


Fig. 6. Schematic of the force exerted into the nozzle.

From the x -momentum conservation equation for this control

volume, the thrust force generated by this propulsion system can be obtained as given in Eq. (9):

$$F_{\text{thrust}} = \dot{m}(V_e) + A_e(P_e - P_a) + F_x, \quad \text{Eq. 9}$$

where the first term on the right-hand side of the equation represents the force produced by the momentum and account for the greater portion of the thrust force. The second term is the pressure thrust, which is related to the force produced by the outlet flow pressure. Fig. 6 shows a thrust nozzle with a conical center body. The figure shows schematically how the pressure forces are applied on the nozzle outlet area and the cone outside the nozzle exit, as well as the momentum at the nozzle exit. In this case, pressure recovery on the cone outside the nozzle exit can generate an additional thrust force. Force F_x is the summation of the pressure and shear forces in the X -axis direction acting on the protruding part of the cone. In this configuration, to calculate the thrust, the force acting on the protruding part of the cone should also be considered. This force was calculated from the following equation:

$$F_x = \int (P_{\text{wall}} - P_a)dA_c + \int \tau dA_y, \quad \text{Eq. 10}$$

where P_{wall} and τ represent the pressure and shear stress applied to the cone's outer part, respectively while A_c and A_y denote the projected area of the cone's outer part on the nozzle exit plane and the horizontal plane, respectively. Since the ambient pressure is constant, P_a was omitted from Eqs. (9) and (10), simplifying the thrust force as follows:

$$F_{\text{thrust}} = \dot{m} V_e + P_e A_e + \int P_{\text{wall}} dA_c + \int \tau dA_y \quad \text{Eq. 11}$$

The performance of a nozzle is evaluated based on the thrust coefficient, which is defined as follows:

$$C_t = \frac{F_{\text{thrust}}}{F_{\text{thrust-ideal}}}, \quad \text{Eq. 12}$$

where the ideal thrust force is associated with an isentropic flow condition. Under this assumption, the pressure at the nozzle exit is exactly equal to the atmospheric pressure, and therefore, the pressure thrust force for ideal conditions becomes zero. Hence, the equation related to the thrust coefficient can be rewritten as follows:

$$C_t = \frac{\int_0^R \left(\rho u^2 + (P - P_{\text{atm}})rdr \right)}{u_{\text{ideal}} \int_0^R \rho u r dr} \quad \text{Eq. 13}$$

The nozzle performance is evaluated based on the thrust coefficient. The closer its value is to one, the greater is the thrust generated—this finding implies less fuel consumption under the same operating conditions. Furthermore, by optimizing the nozzle and increasing its ability to generate thrust, a lightweight nozzle can be designed.

3.2. Constraints, design parameters, and nozzle configurations

a) Optimization constraints

During the optimization process, the inlet and outlet section of the nozzle and the area were kept constant. Considering the stagnation pressure and temperature as the inlet boundary conditions, the mass flow rate was maintained almost constant during the optimization process. Furthermore, the length of the outer wall of the nozzle was held constant to enable a comparison of the results.

b) Design parameters

The profiles of the thrust nozzle's outer wall and conical center body

were parameterized using control points to define curves on them. As a result, geometric parameters such as the nozzle angle at the inlet and outlet, the length of the conical center body, and the type and extent of curvature of the nozzle shell and cone were automatically adjusted during the optimization of the curves of the outer wall and conical center body.

c) Nozzle configurations

Based on the shape of the conical section, three configurations, which are schematically shown in Fig. 7, were considered for the nozzle shape. In the first scenario, the conical center body extended beyond the shell of the nozzle (Fig. 7(a)). In the second scenario, similar to the first case, the conical section was longer than the nozzle shell. However, the inclination of the cone inside and outside the nozzle was positive and negative, respectively. The slope of the cone was nearly negligible at the nozzle exit section, implying that the flow exited the nozzle in a near-horizontal manner (Fig. 7(b)). In the final scenario, the cone was entirely within the nozzle, and its length was consistently shorter than the length of the shell of the nozzle (Fig. 7(c)).

3.3. GA-based topology optimization

GA is a type of optimization search method inspired by Darwin's natural selection and evolution theory. GA has been successfully applied to a wide range of optimization problems, including linear, discrete, and continuous problems. In GA-based optimization, a population of candidate solutions is generated, and it evolves toward an optimal solution, subject to the objective function. The objective function acts as a link between the GA optimizer and the actual problem. During the iterative process of GA-based optimization, the quality of the obtained optimal solution improves with each iteration. The process of reproduction, which includes selection, recombination, and mutation, is repeated until a new generation is generated to replace the previous one. The optimization process can be terminated based on various criteria. Highly fit individuals produce more offspring in the subsequent generations, causing the population as a whole to gradually move toward an optimal solution. GAs do not require an objective function to be differentiable or continuous; they only need the value of the objective function in their search. The primary operators in GA optimization are crossover and mutation. Crossover involves randomly selecting pairs of parents and combining their genetic information, while mutation introduces new, unexplored points into the search domain.

For GA-based topology optimization, it is crucial to parameterize the geometry and introduce it to the optimization algorithm so that the geometry can be changed through the parameters defining the geometry. Parameterizing the geometry provides flexibility in the local modification of the geometry without a complete redesign. Thus, the baseline geometry can be gradually modified to achieve the desired performance. In the first part of this study, the thrust nozzle shape was parameterized using a Bezier curve. A Bezier curve is associated with the vertices of a polygon, where some of these vertices lie on the curve itself. This collection of vertices is referred to as control points or Bezier points. Let's consider the following set of points as control points for a Bezier curve:

$$\mathbf{P} = \{P_0, P_1, P_2, \dots, P_n\} \mid P_i \in \mathbb{R}^2, i=0, \dots, n \quad \text{Eq. 14}$$

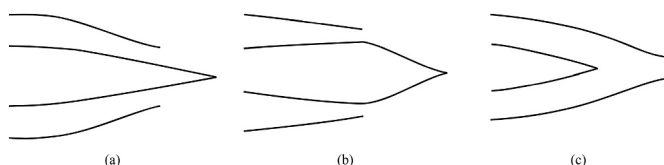


Fig. 7. Three configurations of a transonic thrust nozzle.

The relationship of the Bezier curve, incorporating the points from Eq. (14), is introduced as follows:

$$\mathbf{B}(t) = \sum_{i=0}^n b_{i,n}(t) \mathbf{P}_i \quad i = 0, 1, \dots, n \quad \text{Eq. 15}$$

where t represents the independent parameter, and $b_{i,n}(t)$ denotes Bernstein polynomials, defined as in Eq. (16):

$$b_{i,n}(t) = \binom{n}{i} (1-t)^{n-i} t^i \quad 0 \leq t \leq 1 \quad \text{Eq. 16}$$

where n represents the degree of polynomial, so the number of control points of the Bezier curve is equal to $n+1$ [47].

Fig. 8 depicts an example of a nozzle created by the Bezier curves. To parameterize the thrust nozzle shape, we employed one Bezier curve with five control points for the nozzle shell and another curve with seven control points for its conical center body, as indicated by blue points in Fig. 8. Parameterization of the nozzle shape and its automatic connection with the GA and Fluent solver was performed by coding in MATLAB software.

The optimization process involved defining the fixed and variable geometric constraints, setting the parameters of the GA, creating an initial population, meshing the geometry, solving the flow field using a numerical solver, and calculating the thrust force as the objective function value. Genetic operators such as mutation and crossover were iteratively used to create new generations. The fitness and objective function values of each member were evaluated, and the best members were selected for the next generation. The process continued until the convergence criterion was met.

3.4. Adjoint optimization method

The adjoint method is a gradient-based optimization technique that offers significant advantages in terms of gradient calculation speed, despite its greater complexity compared to the other gradient-based optimization algorithms. In this method, the nodes on the walls of a given geometry act as the input parameters, and the derivative of the objective function relative to each node is calculated. The main advantage of the adjoint method is that the computational cost of calculating the gradient of the design variables is independent of the number of these variables, and the flow and adjoint equations need only be solved once per optimization cycle. Another benefit is that geometric constraints can be easily applied without increasing the computational costs. Adjoint equations can be used in both discrete and continuous schemes. According to Kim et al. [48], the gradients obtained by the adjoint method, in continuous and discrete forms, have high accuracy and are highly consistent with those acquired via the finite difference method.

Based on the author's experience, the sensitivity of the nozzle

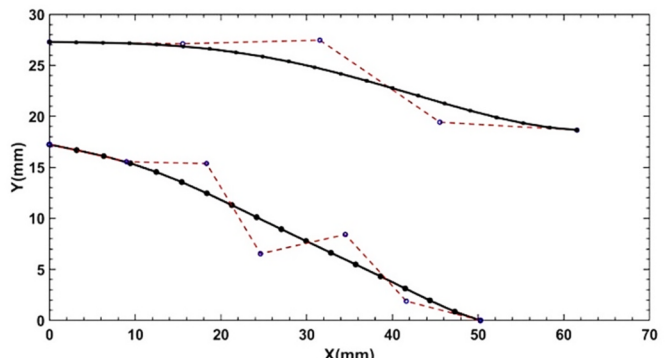


Fig. 8. Sample of nozzle configuration produced by the Bezier curve.

geometry optimized by genetic algorithm (GA) to thrust, when used as the objective function in the adjoint solver, was found to be minimal. Therefore, as the first optimization phase by GA approximately determines the global optimum, the subsequent optimization with the adjoint method aims for further improvement. As a result, the axial velocity variance function at the nozzle outlet was employed as the cost function as follows:

$$\sigma^2 = \frac{\int (V_e - \bar{V}_e)^2 2\pi r dr}{A_e} \quad \text{Eq. 17}$$

where σ^2 is the variance, V_e and \bar{V}_e are local and average axial velocity, respectively, r is the radius variable at the nozzle outlet, and A_e is the nozzle exit area.

Essentially, minimizing the axial velocity variance at the nozzle exit promotes uniformity in the exit velocity profile and maximizes the capacity of flow velocity to generate thrust. Therefore, the adjoint-based optimization minimizes the axial velocity variance of at the nozzle exit as the cost function, denoted by the symbol I . The design parameters are categorized into two types: W , representing flow field variables, and F , representing geometry-related variables. The key insight is that the flow variables (W) are dependent on the geometric variables (F), expressed as $W = W(F)$.

The sensitivity of the cost function with respect to these variables (δI) is then given by:

$$\delta I = \left[\frac{\partial I}{\partial W} \right] \delta W + \left[\frac{\partial I}{\partial F} \right] \delta F \quad \text{Eq. 18}$$

This equation delineates the direct and indirect effects of geometry on the cost function. Utilizing flow governing equations and boundary conditions, a relationship $R(W, F) = 0$ is established. The partial derivative of the relation R is obtained as follows:

$$\delta R = \left[\frac{\partial R}{\partial W} \right] \delta W + \left[\frac{\partial R}{\partial F} \right] \delta F = 0 \quad \text{Eq. 19}$$

The term δR represents the change in $R(W, F)$ due to changes in the flow field variables (W) and geometry-related variables (F). If δR is multiplied by an additional variable ψ^T and subtracted from the sensitivity equation, resulting in:

$$\delta I = \left(\left[\frac{\partial I}{\partial W} \right]^T - \psi^T \left[\frac{\partial R}{\partial W} \right] \right)_I \delta W + \left(\left[\frac{\partial I}{\partial F} \right]^T - \psi^T \left[\frac{\partial R}{\partial F} \right] \right)_II \delta F \quad \text{Eq. 20}$$

To eliminate the dependence on flow parameters (δW), the first term in Eq. (18) should be zero, resulting in:

$$\left[\frac{\partial R}{\partial W} \right]^T \psi = \frac{\partial I}{\partial W} \quad \text{Eq. 21}$$

This yields a simplified expression:

$$\delta I = G \delta F, \quad \text{Eq. 22}$$

where,

$$G = \left[\frac{\partial I}{\partial F} \right] - \psi^T \left[\frac{\partial R}{\partial F} \right] \quad \text{Eq. 23}$$

The variation in the cost function (δI) is not directly influenced by the variation in the geometric parameters (δW). Instead, the impact of δW is reflected in the variation of the flow field (δF). This outcome aligns with the intended goal of having the cost function dependent on geometric parameters. Specifically, the term G is derived by solving the main flow equations and one order of the adjoint equations. Both the adjoint equations and the main flow equations undergo a discretization process. The term δR is closely related to the concept of residuals in the context of solving the flow governing equations and adjoint equations. Residuals are typically measures of the errors in these equations, representing the

discrepancies between the computed and expected values.

In the current study, the adjoint solver in Fluent 2022 R2 software was used for nozzle topology optimization. This module adopts a discrete approach that offers high levels of accuracy and versatility, making it suitable for a broad range of problems. In the adjoint optimization procedure, the focus is on a particular region of the flow with a border characterized by multiple control points. The goal is to optimize the positions of these control points iteratively using adjoint equations, ultimately achieving an optimal shape of the wall. A hybrid approach involving Bezier curves and Bernstein polynomials was used to parameterize the geometry in the adjoint module in the Fluent. Both techniques were used to translate the movement of control points into surface profile modification. The movement of control points associated with Bernstein polynomials facilitates changes on a broader scale, whereas that of control points linked to Bezier curves limits changes on a smaller scale.

The nozzle geometry obtained from the GA-based optimization was meshed and then imported into Fluent. By setting the boundary conditions in Fluent, the governing equations of the flow were numerically solved. For optimizing the geometry of the nozzle along each of the coordinate axes, 25 control points have been considered, and optimization also has been performed over 15 iterations. After the numerical solution, the cost function was defined for solving the adjoint equations. First-order methods were used for discretizing the adjoint equations to facilitate convergence. The optimization tool then used the gradients obtained from solving the adjoint equations to suggest changes to the geometry. After these changes were made, the mesh was adjusted so that it was proportional to the new geometry; finally, a new geometry was obtained. The flow equations for the new nozzle were solved, and the degree of change in the cost function was examined. If the cost function reached the desired limit, the optimization was stopped; otherwise, the optimization cycle was repeated.

4. Results and discussion

As shown in Fig. 7, the nozzle geometry was classified into three distinct configurations corresponding to the shape of the conical section. Individual optimization procedures were executed for each configuration. Subsequently, the optimized cases within each configuration were compared to determine the most optimal nozzle configuration.

The GA was used to explore the search space to realize a geometry close to the global optimum. The setting parameters in the GA, including the number of control points, initial population size, number of generations, and the total number of generated geometries for the three configurations, are summarized in Table 4. Fig. 9 shows the evolutionary trends of the best solution in each generation, illustrating the convergence toward maximizing the thrust force for the three configurations. There was a significant increase in the propulsive force in the initial generations; thereafter, there was a gradual slowdown in the rate of increase, eventually leading to convergence. The rate of improvement reached a point where the value of the objective function remained unchanged in the last generations. This phenomenon, commonly observed in GAs, implies that the algorithm has likely converged to a

Table 4
Setting parameters in the genetic algorithm (GA) for the three configurations.

Setting parameters in GA	First configuration	Second configuration	Third configuration
Number of control points on the outer wall	5	5	5
Number of control points on conical surface	7	7	7
Initial population	60	60	60
Number of generations	25	25	15
Number of generated geometries	1410	1410	870

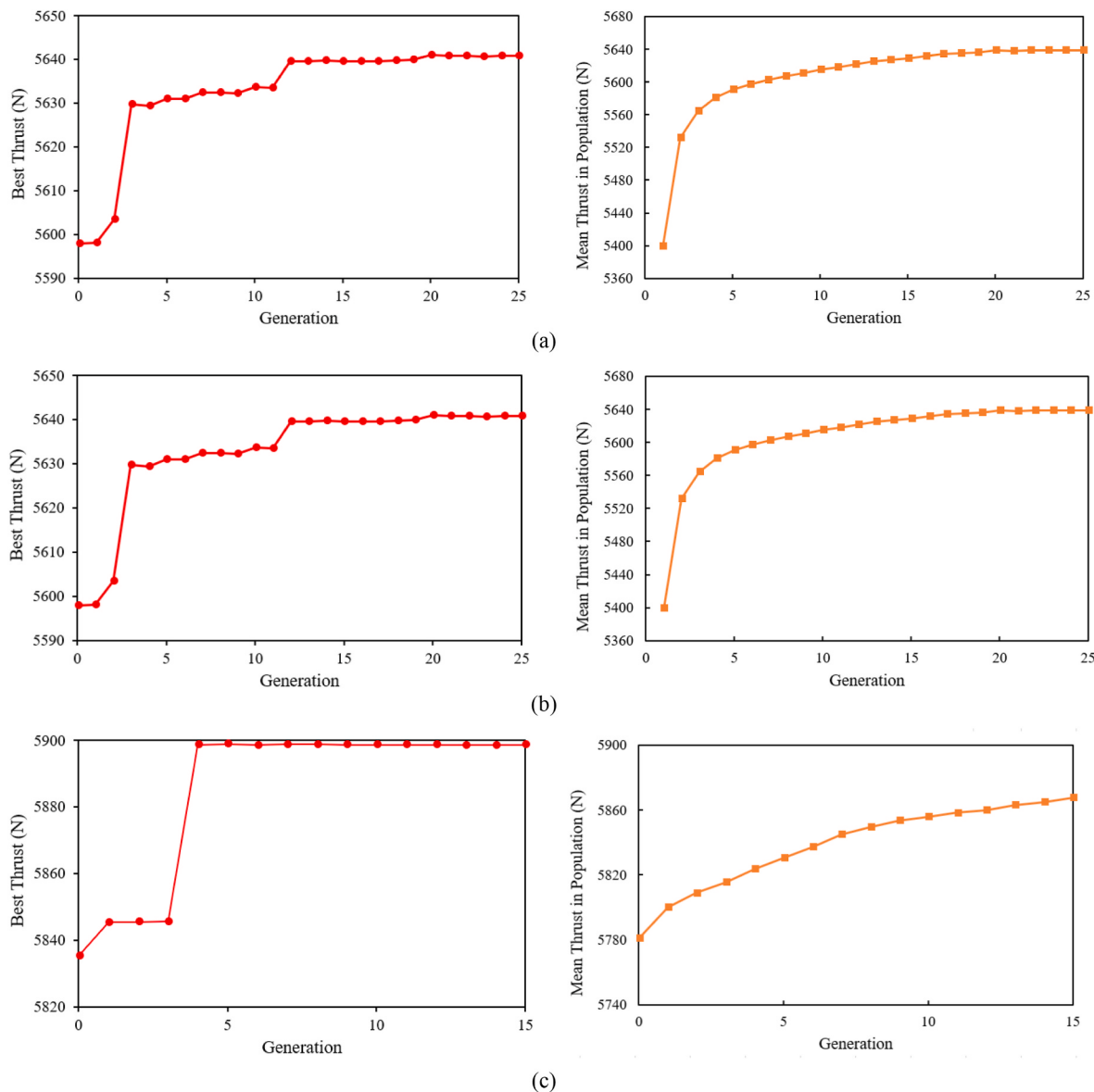


Fig. 9. Changes in the best and average propulsive forces across iterations of the GA for (a) the first, (b) second, and (c) third configurations.

local optimum or a near-optimal solution, making further progress challenging. The criterion for the convergence of optimization in a genetic algorithm (GA) typically relies on monitoring the best values rather than the mean values. In all configurations depicted in Fig. 9, it is evident that the best values remain largely unchanged in the final few generations generated. This phenomenon was also evident in the mean values in each generation.

The geometry obtained after GA-based optimization was further optimized using the adjoint method to achieve a better geometry and increase the thrust force. For varying the nozzle geometry, 25 control points were considered along each coordinate axis. Fig. 10 illustrates the adjoint-based optimization process, where the axial velocity variance, serving as the cost function, undergoes minimization across 15 optimization iterations.

Fig. 11 shows the geometries obtained by GA-based optimization, adjoint optimization, and the weakest identified geometry in the GA for the three configurations. The weakest geometry in terms of propulsive force was adopted as the baseline geometry only for comparison and for establishing the performance of the baseline geometry. Fig. 11(a) shows that throughout the optimization process, the cone protruding from the nozzle exit section gradually moves closer to the nozzle exit, which is

similar to the optimized geometry for the third configuration (Fig. 11(c)). This observation indicates that a shorter protruded length in the nozzle leads to greater thrust force compared to configurations with longer protrusions (as indicated in Tables 5 and 6). Importantly, this theory finds support in a study conducted by Khare and Saha [49], where it is noted that a truncated nozzle yields a larger thrust force compared to a conical nozzle (see Table 7).

As the adjoint method was primarily used to find the local optima, it generally induced partial modifications and limited changes in the geometry. A comparison of the geometries obtained from the GA-based and adjoint optimization process confirms this observation. The most significant corrections induced by the adjoint method were concentrated near the nozzle outlet so that the nozzle wall slope at the exit plane could be changed for all three configurations. In fact, Rapid changes in the slope near the outlet section indicate that the cross-section near the outlet is decreasing for adjoint optimization. In other words, the adjoint optimization attempts to drastically reduce the cross-sectional area of the nozzle near its exit with the aim of maintaining a low flow velocity within the nozzle and allowing the velocity to increase as the flow approaches the exit. The main differences between the optimized and baseline geometries in the first configuration showed a decrease in the

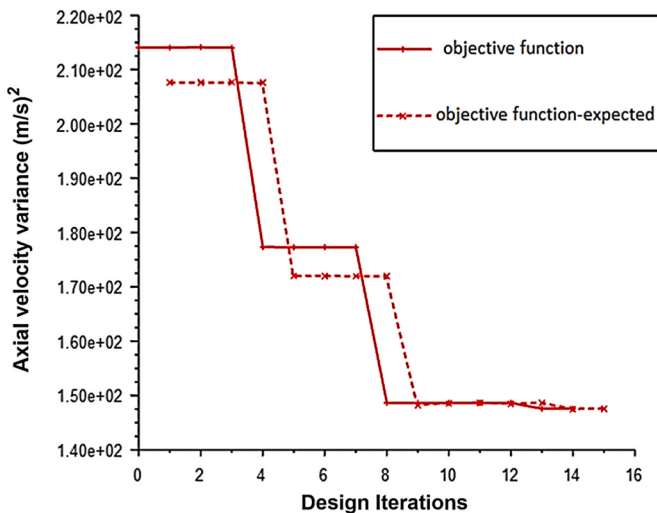


Fig. 10. Evolution of the cost function variations over the iterations of the adjoint optimization method.

conical section length, a change in its curvature, and a decrease in the radius of the nozzle exit plane. In the second configuration, the length of the conical section was increased compared to the first section to reduce the slope of the cone outside the nozzle; moreover, the radius of the exit plane of the nozzle was slightly reduced. In the third configuration, the cross-sectional areas within the nozzle of the adjoint-optimized design were greater than those of the GA-optimized design. Additionally, the cross-sectional areas within the nozzle for both optimized designs exceeded those of the baseline geometry.

To understand the correlation between changes in geometry and the consequent enhancement in propulsive force, it is essential to examine the flow properties. Fig. 12 shows the contours of the Mach number for the initial, GA-optimized, and adjoint-optimized nozzles across the three configurations. The Mach number reached approximately 0.95 at the nozzle exit for all the optimized geometries, though it was slightly less than this value for the initial nozzles. GA optimization and optimization by the adjoint method for the three configurations reduced the flow velocity inside the nozzle. Nonetheless, the reduction in velocity was more pronounced in the case of the adjoint-optimized nozzles. Moreover, the regions characterized by low velocities adjacent to the conical center body of the initial nozzles shrunk or disappeared through optimization across all configurations so that the flow velocity downstream of the nozzle and in the vicinity of its axis increased in both optimization

steps. The intense changes in velocity near the exits of the adjoint-optimized nozzles were related to the higher slope of the nozzle walls at the exit plane.

Fig. 13 shows the Mach number distributions at the exit of the initial, GA-optimized, and adjoint-optimized nozzles across all configurations. For both types of optimized nozzles, the exit velocity was reduced and the velocity was more evenly distributed compared to the initial nozzle in all configurations. The most uniform velocity was observed in the case of the adjoint-optimized nozzle. In the first and third configurations (Fig. 13(a) and (c)), the adjoint optimization caused an increase in the

Table 5

Output parameters of the initial, GA-optimized, and adjoint-optimized nozzles for the first configuration.

Output parameters	Initial nozzle	GA-optimized	Adjoint-optimized
Average gauged outlet pressure (Pa)	1112.8	8508.2	8050.7
Average outlet velocity (m/s)	304.5	290.5	292.3
Mass flow rate (kg/s)	18.42	18.63	18.7
Thrust force (N)	5645.2	5810	5841

Table 6

Output parameters of the initial, GA-optimized, and adjoint-optimized nozzles for the second configuration.

Output parameters	Initial nozzle	GA-optimized	Adjoint-optimized
Average gauged outlet pressure (Pa)	-6311	2835	3620.7
Average outlet velocity (m/s)	319.3	302.2	300.9
Mass flow rate (kg/s)	18.1	18.5	18.6
Thrust force (N)	5192	5708	5732.6

Table 7

Output parameters of the initial, GA-optimized, and adjoint-optimized nozzles for the third configuration.

Output parameters	Initial nozzle	GA-optimized	Adjoint-optimized
Average gauged outlet pressure (Pa)	236.6	6996.5	7770.7
Average outlet velocity (m/s)	307.05	293.9	292.86
Mass flow rate (kg/s)	18.45	18.6	18.66
Thrust force (N)	5677	5796.7	5829.7

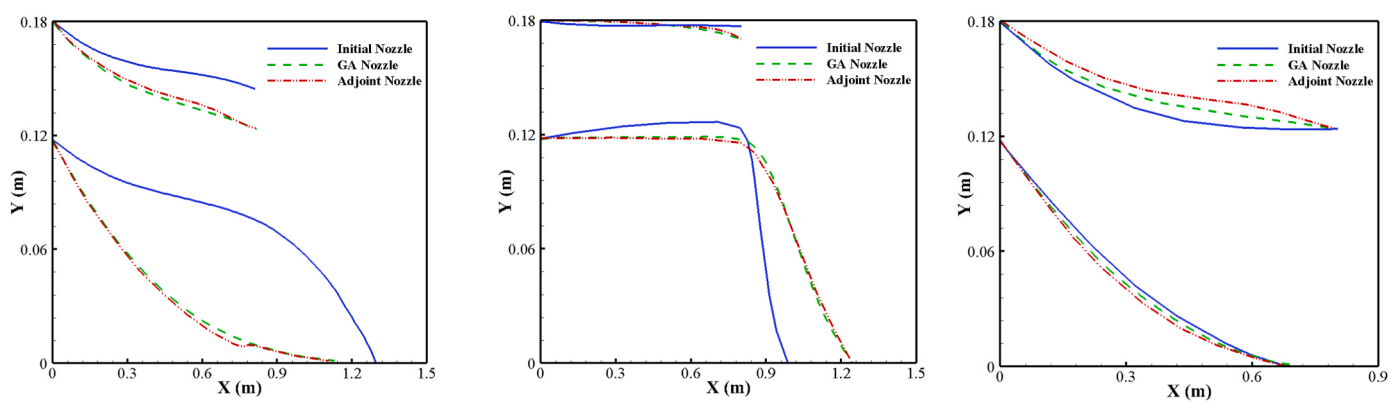


Fig. 11. Comparison of the nozzle geometry profiles of the initial, GA-optimized, and adjoint-optimized geometries for the (a) first, (b) second, and (c) third configurations.

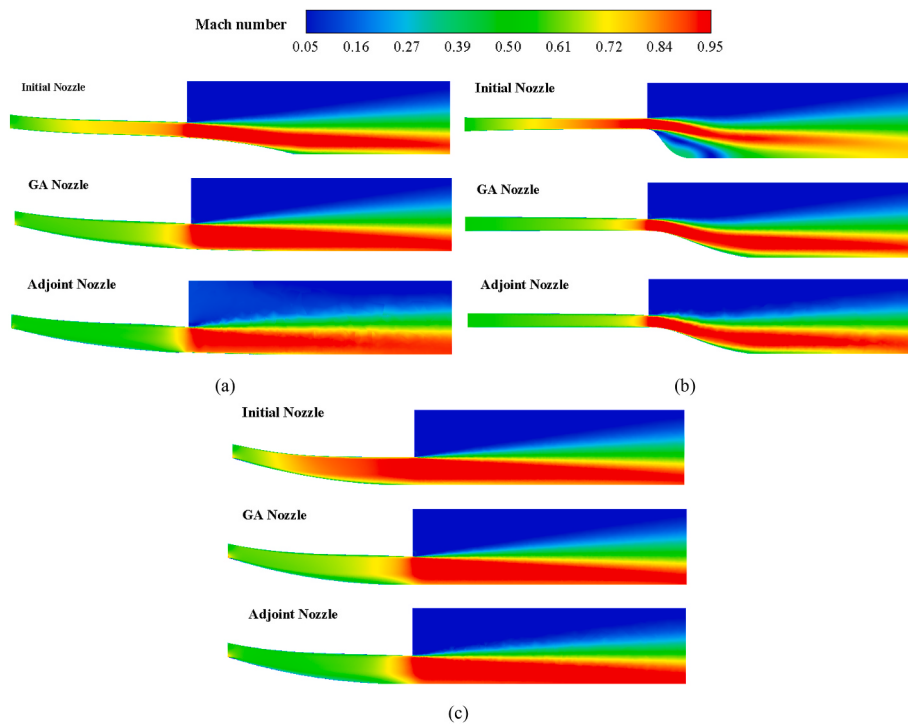


Fig. 12. Mach number contours inside and outside the initial, GA-optimized, and adjoint-optimized nozzles for the (a) first, (b) second, and (c) third configurations.

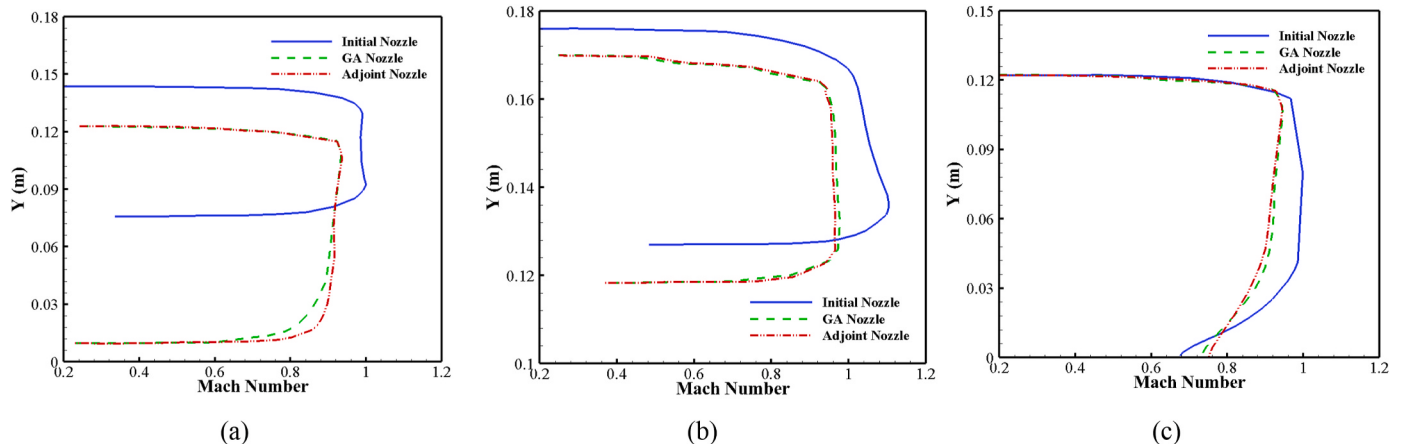


Fig. 13. Mach number distributions on the exit sections of the initial, GA-optimized, and adjoint-optimized nozzles for the (a) first, (b) second, and (c) third configurations.

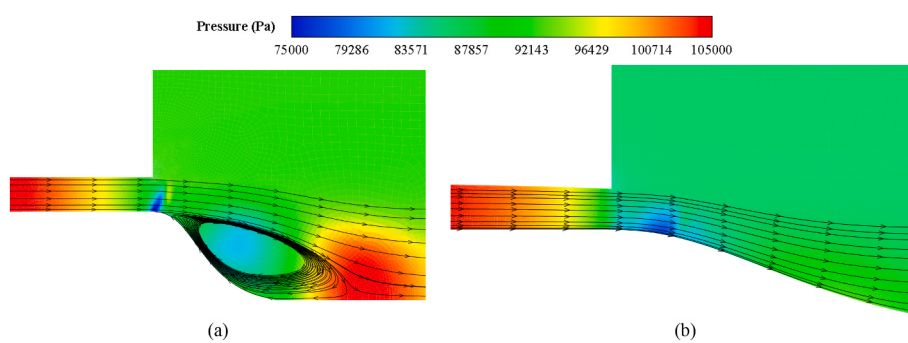


Fig. 14. Streamlines on the conical surfaces of the (a) initial and (b) GA-optimized nozzles for the second configuration.

velocity in the vicinity of the conical central part of the body at the exit plane, resulting in a more uniform velocity distribution.

Fig. 13(b) reveals that the Mach number at the exit of the initial nozzle exceeds unity; this result is attributed to the high curvature of the convex wall of the conical center body after the exit plane. The intense change in the direction of the curvature of the conical surface creates a strong adverse pressure gradient and flow separation on the cone, as shown in **Fig. 14(a)**. In both GA-optimized and adjoint-optimized nozzles, the curvature of the conical surface was reduced, causing the flow separation to disappear, as shown in **Fig. 14(b)**.

Fig. 15 compares the static pressure distributions at the exit plane of the initial, GA-optimized, and adjoint-optimized nozzles for all configurations. Both optimization steps resulted in enhanced static pressure at the outlet, consequently increasing the density and pressure thrust. Nevertheless, among the three configurations, the adjoint-optimized nozzle exhibited the highest outlet pressure.

Fig. 16 shows the pressure contours inside the initial, GA-optimized, and adjoint-optimized nozzles across all configurations. Both optimization methods led to enhanced static pressure within the nozzle because of the increased cross-sectional areas of the nozzle. Notably, the adjoint optimization yielded the highest internal static pressure within the nozzle for the second and third configurations in contrast to the first one, where the GA optimization has the highest one.

Fig. 17 shows the static pressure distributions along the outer walls of the initial, GA-optimized, and adjoint-optimized nozzles across all configurations. Both optimization methods led to enhanced static pressure within the nozzle because of the increased cross-sectional areas of the nozzle. Notably, this figure also shows that the adjoint optimization yielded the highest internal static pressure within the nozzle for all configurations. The sudden pressure reduction at the outlet of the adjoint-optimized nozzle is attributed to the drastic change in the slope of the nozzle wall at the exit plane.

Under the ideal isentropic condition, neglecting the downstream flow, the estimated pressure at the nozzle exit is zero; however, under actual conditions, this pressure is greater than zero. In other words, both components of the propulsive force—pressure and momentum—exist. The fundamental challenge in nozzle optimization is to balance these components to maximize the resultant propulsive force; these components are interconnected, and reducing one leads to an increase in the other, and vice versa. Consequently, it is necessary to realize a geometry in which the pressure and velocity at the nozzle exit are configured such that maximizes the combined propulsive force. In the genetic optimization step, geometry alteration initially led to a remarkable increase in pressure and a reduction in velocity at the exit. Subsequently, the partial correction applied by the adjoint method further modified the pressure and momentum components, leading to an increase in the overall

propulsive force. In addition to the aforementioned factors, another critical factor in the optimization of the propulsive force is the magnitude of viscous losses in the flow. A reduction in viscous losses can lead to improved nozzle performance. The drop in stagnation pressure along the nozzle wall signifies losses due to frictional flow. Therefore, reducing the flow velocity within the nozzle can reduce the frictional losses and enhance stagnation pressure.

Fig. 18 shows the stagnation pressure distributions along the outer walls of the initial, GA-optimized, and adjoint-optimized nozzles across all configurations. As observed, both optimization steps led to an enhanced stagnation pressure along the nozzle wall. Hence, in the optimized nozzles, the stagnation pressure at the outlet was higher than that in the initial nozzle. This result implies that the frictional losses decreased upon optimization. The adjoint-optimized nozzle yielded the highest stagnation pressure for all configurations.

Fig. 19 shows the contours of entropy within the initial, GA-optimized, and adjoint-optimized nozzles for all configurations. In the flow inside the nozzle, the nozzle walls were assumed to be adiabatic, and no heat transfer occurred from the walls. Therefore, viscous losses are the only cause of the creation of high-entropy regions near the walls. A comparison of the contour plots corresponding to the initial and optimized nozzles clearly showed that the two optimization steps led to lower viscous losses. This phenomenon can be more clearly observed in **Figs. 20 and 21**, which show the entropy distribution along the outer wall and conical surface of the nozzle, respectively.

Table 5, **6**, and **7** summarize the integral output parameters of the initial, GA-optimized, and adjoint-optimized nozzles for the first, second, and third configurations, respectively. In the following tables, the gauged outlet pressure represents the pressure relative to atmospheric pressure, and also the average shows the mean of the value over the exit cross-section. Both optimization steps caused a reduction in the average velocity and an increase in the average pressure at the nozzle exit, enhanced the mass flow rate, and ultimately, increased the thrust force. **Table 8** shows a comparison of the thrust coefficient and improvement percentage for the GA and adjoint optimizations relative to the initial nozzle for all configurations. According to this table, the highest thrust coefficient was achieved for the first configuration, in which the conical surface was positioned slightly beyond the nozzle exit.

5. Conclusion

This study focused on optimizing the topology of a convergent thrust nozzle with a conical center body. The approach combined a GA as a metaheuristic tool with an adjoint method as a gradient-based technique. The optimization process comprised two stages: the GA initially approximated a global optimum, and subsequently, the adjoint method

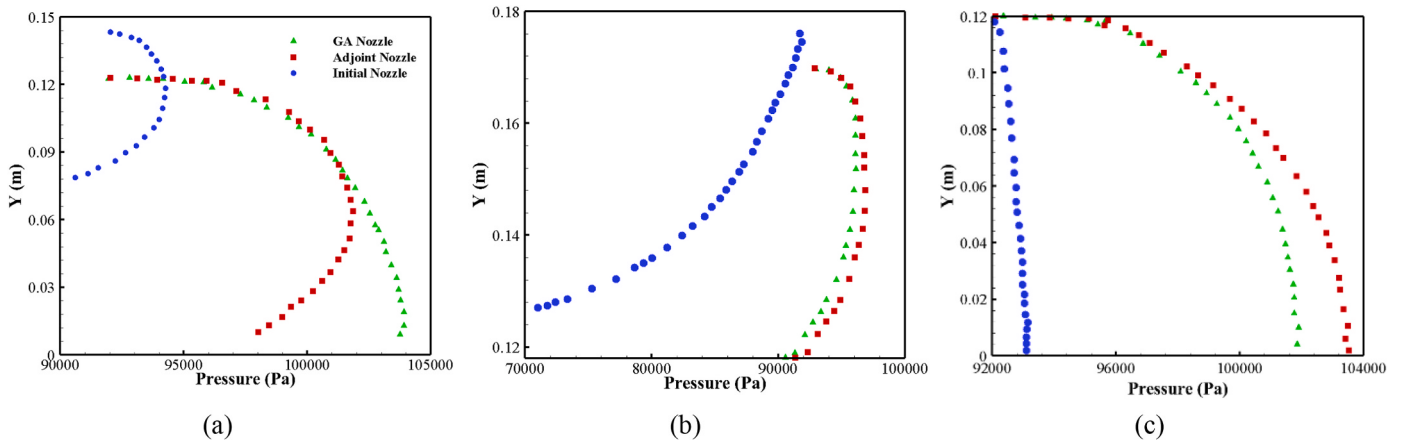


Fig. 15. Static pressure distributions on the exit sections of the initial, GA-optimized, and adjoint-optimized nozzles for the (a) first, (b) second, and (c) third configurations.

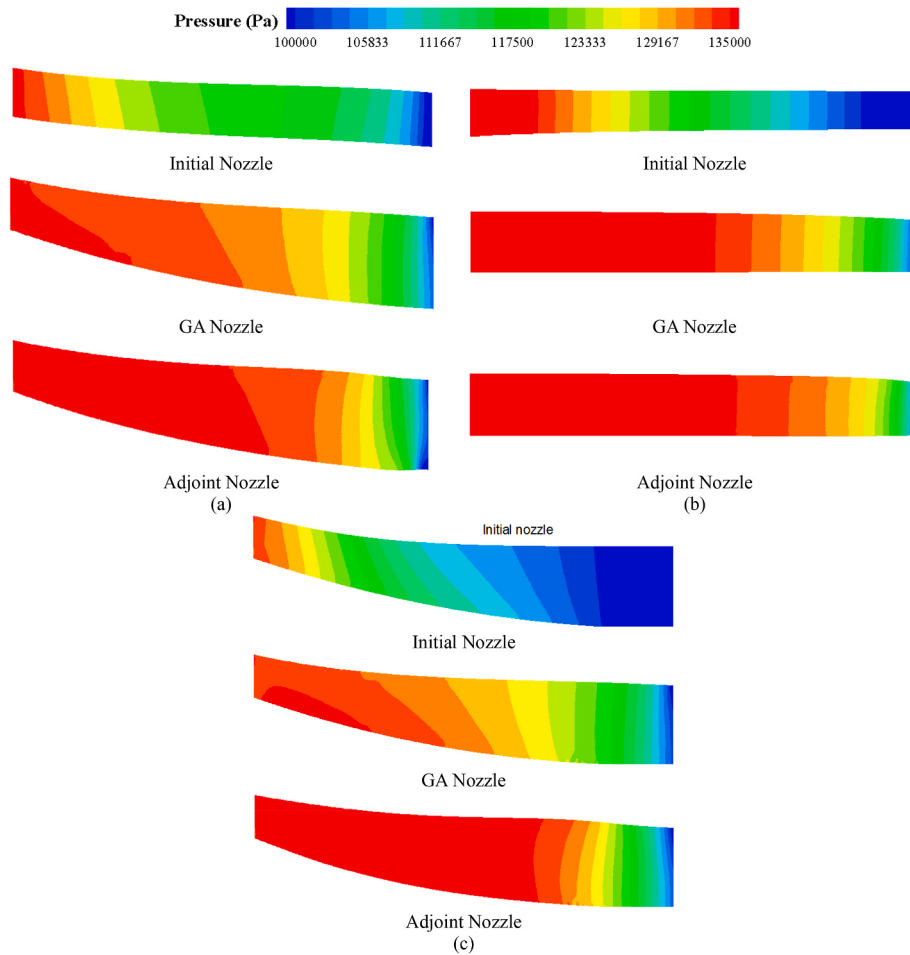


Fig. 16. Contours of the Mach number inside and outside the initial, GA-optimized, and adjoint-optimized nozzles for the (a) first, (b) second, and (c) third configurations.

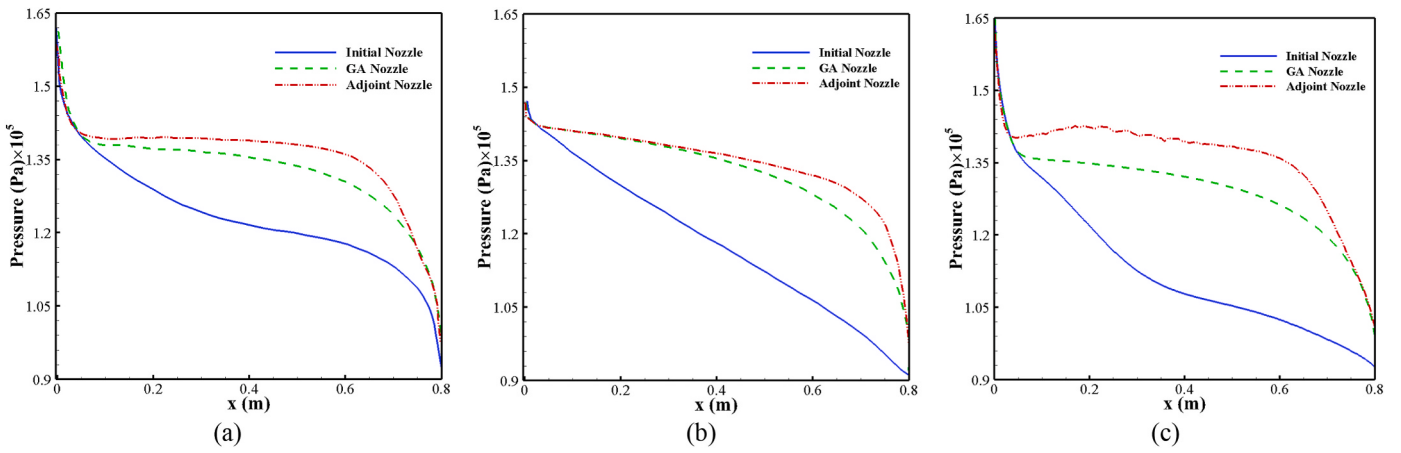


Fig. 17. Static pressure distributions on the outer walls of the initial, GA-optimized, and adjoint-optimized nozzles for the (a) first, (b) second, and (c) third configurations.

was used for precise refinement. The genetic algorithm aimed to maximize the thrust coefficient as the objective function, while the adjoint solver aimed to minimize the axial velocity variance at the nozzle outlet as the cost function. Three axisymmetric nozzle configurations based on the position of the conical center body were considered in the GA-based optimization. The geometry of the outer walls and conical surface of the nozzle was parameterized using the Bezier curve. For mesh generation,

Gambit software was used. Fluent 2022R2 software was used to solve the two-dimensional axisymmetric Reynolds-averaged Navier–Stokes equations for evaluating the thrust force as the objective function. A MATLAB code was used for geometry parameterization and to connect the GA, meshing software, and flow solver. The key findings from the nozzle optimization study are summarized as follows.

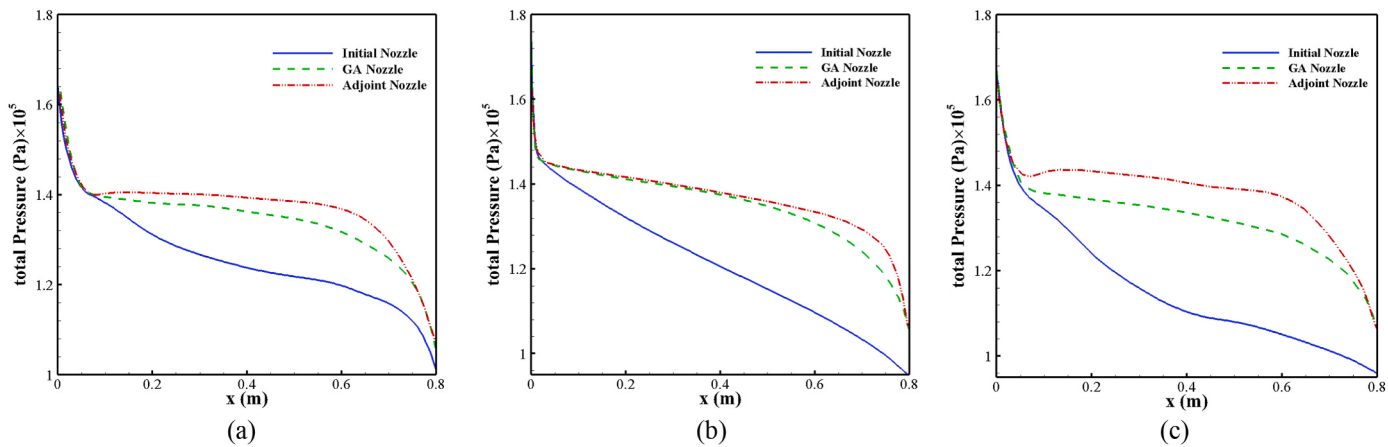


Fig. 18. Stagnation pressure distributions on the outer walls of the initial, GA-optimized, and adjoint-optimized nozzles for the (a) first, (b) second, and (c) third configurations.

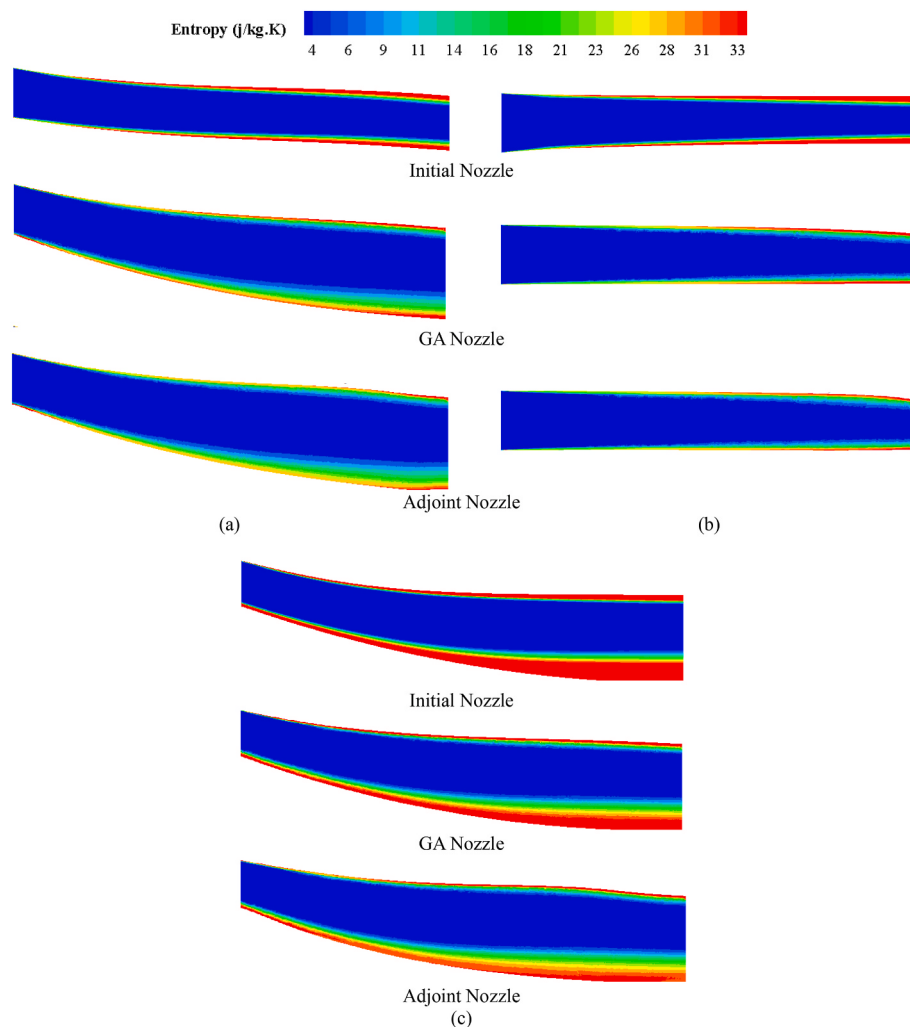


Fig. 19. Entropy contours inside and outside the initial, GA-optimized, and adjoint-optimized nozzles for the (a) first, (b) second, and (c) third configurations.

- Both optimization stages increased the cross-sectional area within the nozzle and outer wall slope at the exit, thereby increasing exit pressure.
- Both optimization stages reduced the average exit velocity, established a uniform velocity distribution at the nozzle exit, and

increased the velocity along the conical surface downstream of the nozzle exit and near the axisymmetric line.

- Both optimization stages reduced the velocity within the nozzle, thereby decreasing frictional velocity losses, stagnation pressure losses, and entropy generation near the wall.

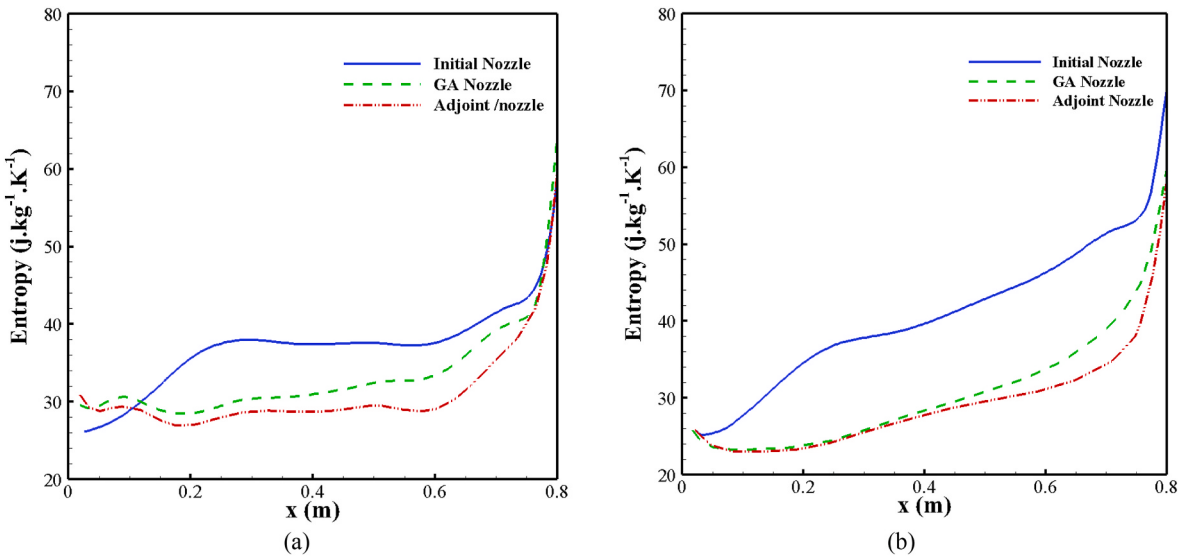


Fig. 20. Entropy distributions on the cone wall of the initial, GA-optimized, and adjoint-optimized nozzles for the (a) first and (b) second configurations.

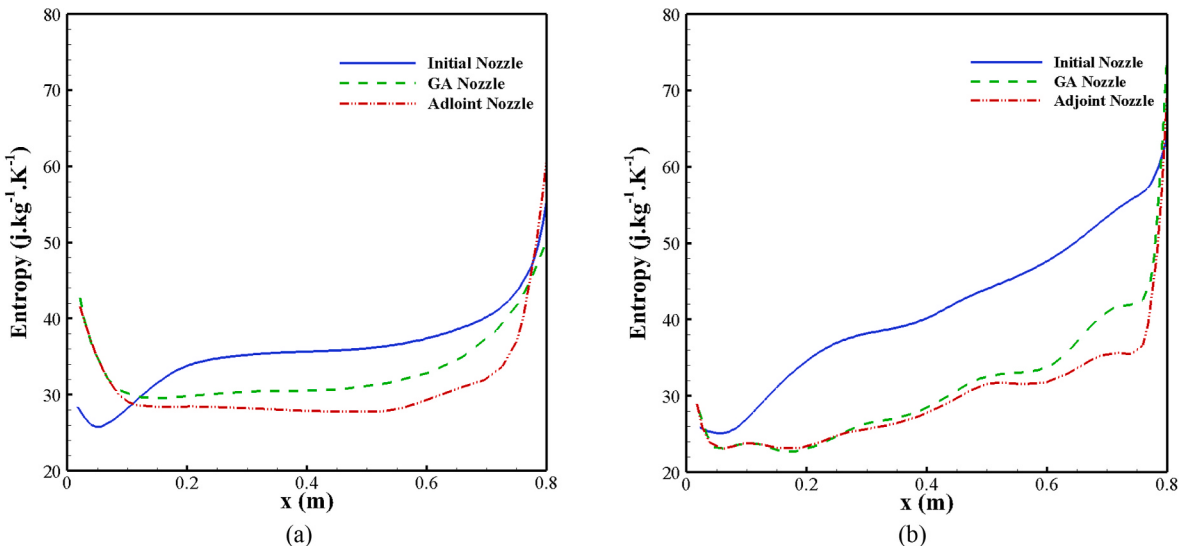


Fig. 21. Entropy distributions on the outer wall of the initial, GA-optimized, and adjoint-optimized nozzles for the (a) first and (b) second configurations.

Table 8

Comparison of the final thrust coefficients and improvement percentage obtained by GA and adjoint optimizations for the three configurations.

	Optimal thrust coefficient (C_t)	Increase in C_t by GA (%)	Increase in C_t by adjoint (%)
First configuration	96.15	2.92	0.55
Second configuration	94.36	9.94	0.48
Third configuration	95.96	2.11	0.58

- The highest thrust force was achieved when a small portion of the conical center body protruded from the nozzle shell, and in this situation, the slope of the conical surface was negative both inside and outside the nozzle.
- The configurations in which the conical center body protruded from the nozzle shell and had a steep slope downstream of the exit led to flow separation and reduced thrust force.

➤ Thrust force increased by 3 % and 0.6 % because of the optimization by the GA and adjoint method, respectively, resulting in an overall efficiency of 96.15 % for the final optimized nozzle.

This study demonstrated the potential of combining exploratory optimization techniques and gradient-based methods and also clarified the mutual influence between geometry corrections and propulsion enhancement. The obtained optimization results, which are notable because of the increased thrust force and improved efficiency, indicate the practical relevance of this work toward building more efficient and high-performance propulsion systems.

CRediT authorship contribution statement

Younes Narimani: Writing – original draft, Software, Methodology, Investigation, Formal analysis. **Amir Joulaei:** Writing – review & editing, Writing – original draft, Investigation, Formal analysis. **Ahmad Shirvani:** Software, Methodology, Formal analysis, Validation. **Mahdi Nili-Ahmababadi:** Writing – review & editing, Writing – original draft, Supervision, Project administration, Methodology, Formal analysis,

Conceptualization. **Man Yeong Ha:** Supervision, Resources, Project administration.

Declaration of competing interest

The authors declare that they have no known competing financial interests or personal relationships that could have appeared to influence the work reported in this paper.

Data availability

Data will be made available on request.

Acknowledgments

This research was supported by the Brain Pool program funded by the Ministry of Science and ICT through the National Research Foundation of Korea (No. NRF-2022H1D3A2A02063642). This research was also supported by the National Research Foundation of Korea (NRF) grant funded by the Korean government (No. NRF-2019R1A5A8083201). The authors also thank the Isfahan University of Technology for their financial support.

References

- [1] M. Goeing, Nozzle design optimization by method-of characteristics, in: 26th Joint Propulsion Conference, July 1990, pp. 16–18. Orlando, FL.
- [2] B. Mohammadi, O. Pironneau, Applied Shape Optimization for Fluids, OUP Oxford, 2009.
- [3] A. Jameson, Re-engineering the design process through computation, *J. Aircraft* 36 (1) (1999) 36–50.
- [4] J.J. Reuther, A. Jameson, J.J. Alonso, M.J. Rimlinger, D. Saunders, Constrained multipoint aerodynamic shape optimization using an adjoint formulation and parallel computers, part 2, *J. Aircraft* 36 (1) (1999) 61–74.
- [5] J. Reuther, J.J. Alonso, M.J. Rimlinger, A. Jameson, Aerodynamic shape optimization of supersonic aircraft configurations via an adjoint formulation on distributed memory parallel computers, *Comput. Fluid* 28 (4) (1999) 675–700.
- [6] G.V.R. Rao, Exhaust nozzle contour for optimum thrust, *J. Jet Propuls.* 28 (6) (1958) 377–382.
- [7] N.I. Tillyaeva, Comparison of the efficiencies of spike and combined annular nozzles, *Fluid Dynam.* 52 (4) (2017) 587–598.
- [8] D. Davidenko, Y. Eude, F. Falempin, in: Numerical study on the annular nozzle optimization for rocket application, in: 16th AIAA/DLR/DGLR International Space Planes and Hypersonic Systems and Technologies Conference, 2009.
- [9] A.L. Kartashev, M.A. Kartasheva, Profiling of optimal annular nozzles with polyphase working medium, in: 29th Congress of the International Council of the Aeronautical Sciences, 2014. St. Petersburg, Russia.
- [10] C. Jéger, A. Veress, Novel application of CFD for rocket engine nozzle optimization, *Period. Polytech. Transp. Eng.* 47 (2) (2019) 131–135.
- [11] H. Ogawa, R.R. Boyce, Nozzle design optimization for axisymmetric scramjets by using surrogate-assisted evolutionary algorithms, *J. Propul. Power* 28 (6) (2012) 1324–1338.
- [12] K. Ezhilshabareesh, S.H. Rhee, A. Samad, Shape optimization of a bidirectional impulse turbine via surrogate models, *Engineering Applications of Computational Fluid Mechanics* 12 (1) (2018) 1–12.
- [13] A.A. Kraiko, K.S. Pyankov, N.I. Tillyaeva, Contouring two-sided asymmetric plane maximum-thrust nozzles, *Fluid Dynam.* 51 (1) (2016) 120–125.
- [14] G. Bletsos, N. Kuhl, T. Rung, Adjoint-based shape optimization for the minimization of flow-induced hemolysis in biomedical applications, *Engineering Applications of Computational Fluid Mechanics* 15 (1) (2021) 1095–1112.
- [15] L. Da, L. Hanan, Y. Zhe, P. Tianyu, D. Hai, L. Qiushi, Optimization of a transonic axial-flow compressor under inlet total pressure distortion to enhance aerodynamic performance, *Engineering Applications of Computational Fluid Mechanics* 14 (1) (2020) 1002–1022.
- [16] G.V.R. Rao, Approximation of optimum thrust nozzle contour, *ARS J.* 30 (6) (1960) 561.
- [17] G.V.R. Rao, J.E. Beck, T.E. Booth, Nozzle optimization for space-based vehicles, in: 35th Joint Propulsion Conference and Exhibit, June, 1999.
- [18] J.G. Allman, J.D. Hoffman, Design of maximum thrust nozzle contours by direct optimization methods, *AIAA J.* 19 (6) (1981) 750–751.
- [19] L.E. Sternin, Analysis of the thrust characteristics of jet nozzles designed by various methods, *Fluid Dynam.* 35 (1) (2000) 123.
- [20] M. Nili-Ahmabadi, F. Aghabozorgi, D.S. Cho, K.C. Kim, Development and validation of a hybrid aerodynamic design method for curved diffusers using genetic algorithm and ball-spine inverse design method, *Alex. Eng. J.* 60 (3) (2021) 3021–3036.
- [21] X.Q. Xing, M. Damodaran, Design of three-dimensional nozzle shapes using hybrid optimization techniques, in: 42nd AIAA Aerospace Sciences Meeting and Exhibit, 2004.
- [22] G. Cai, J. Feng, X. Xu, M. Liu, Performance prediction and optimization for liquid rocket engine nozzle, *Aero. Sci. Technol.* 11 (2007) 155–162.
- [23] K.O. Mon, C. Lee, Optimal design of supersonic nozzle contour for altitude test facility, *J. Mech. Sci. Technol.* 26 (8) (2012) 2589–2594.
- [24] M. Yumusak, S. Eyi, Design optimization of rocket nozzles in chemically reacting flows, *Comput. Fluid* 65 (2012) 25–34.
- [25] M. Yumusak, Analysis and design optimization of solid rocket motors in viscous flows, *Comput. Fluid* 75 (2013) 22–34.
- [26] K. Yu, X. Yang, Z. Mo, Profile design and multifidelity optimization of solid rocket motor nozzle, *J. Fluid Eng.* 136 (2014) 031104.
- [27] D. Davidenko, Y. Eude, F. Falempin, Optimization of supersonic axisymmetric nozzles with a center body for aerospace propulsion, *Progress in Propulsion Physics* 2 (2011) 675–692.
- [28] K.N. Kumar, M. Gopalsamy, D. Antony, R. Krishnaraj, C.B. V Viswanadhi, Design and optimization of aerospike nozzle using CFD, in: IOP Conference Series: Materials Science and Engineering, 2017.
- [29] F.J. Granados-Ortiz, P. Morales-Higueras, J. Ortega-Casanova, 3D CFD simulation of the interaction between front wheels&brake ducts and optimised five-element F1 race car front wings under regulations, *Alex. Eng. J.* 69 (2023) 677–698.
- [30] A. Jameson, Aerodynamic design via control theory, *J. Sci. Comput.* 3 (3) (1988) 233–260.
- [31] A. Jameson, Automatic design of transonic airfoils to reduce the shock induced pressure drag, in: In Proceedings of the 31st Israel Annual Conference on Aviation and Aeronautics, 1990. Tel Aviv.
- [32] A. Jameson, Optimum aerodynamic design via boundary control, NASA Ames Research Center, Research Institute for Advanced Computer Science 94 (1994).
- [33] A.H. Hassan Saeed, A.M. Nagib Elmekawy, S.Z. Kassab, Numerical study of improving Savonius turbine, *Alex. Eng. J.* 58 (2) (2019) 429–441.
- [34] A. Iollo, M.D. Salas, S. Taasan, Shape optimization governed by the Euler equations using an adjoint method, INSTITUTE FOR COMPUTER APPLICATIONS IN SCIENCE AND ENGINEERING HAMPTON VA, 1993.
- [35] M.B. Giles, N.A. Pierce, On the properties of solutions of the adjoint Euler equations, *Numer. Methods Fluid Dyn.* (1998) 1–16. VI. ICFD.
- [36] E.M. Cliff, M. Heinkenschloss, A.R. Shenoy, An optimal control problem for flows with discontinuities, *J. Optim. Theor. Appl.* 94 (2) (1997) 273–309.
- [37] O. Soto, R. Löchner, C. Yang, An adjoint-based design methodology for CFD problems, *Int. J. Numer. Methods Heat Fluid Flow* 14 (6) (2004) 734–759.
- [38] B. Yerlikaya, E. Leblebici, L. Unlusoy, I.H. Tuncer, Nozzle optimization using adjoint-based optimization tool, in: 31st International Conference on Parallel Computational Fluid Dynamics, Antalya TURKEY, 2019.
- [39] F.R. Menter, M. Kuntz, R. Langtry, Ten years of industrial experience with the SST turbulence model, *Turbul. Heat Mass Transfer* 4 (1) (2003) 625–632.
- [40] F.R. Menter, Performance of popular turbulence model for attached and separated adverse pressure gradient flows, *AIAA J.* 30 (8) (1992) 2066–2072.
- [41] B.E. Launder, N.D. Sandham, Closure Strategies for Turbulent and Transitional Flows, Cambridge University Press, 2002.
- [42] A.K. Mubarak, P.S. Tide, Design of a double parabolic supersonic nozzle and performance evaluation by experimental and numerical methods, *Aircraft Eng. Aero. Technol.* 91 (1) (2018) 145–156.
- [43] F. Orzano, J. Braun, B.H. Saracoglu, G. Paniagua, Multi-stage nozzle-shape optimization for pulsed hydrogen-air detonation combustor, *Adv. Mech. Eng.* 9 (2) (2017) 1–9.
- [44] H. Miaosheng, Q. Lizi, L. Yu, Numerical investigation of flow separation behavior in an over-expanded annular conical aerospike nozzle, *Chin. J. Aeronaut.* 28 (4) (2015) 983–1002.
- [45] P.P. Nair, A. Suryan, H.D. Kim, Computational study on flow through truncated conical plug nozzle with base bleed, *Propulsion and Power Research* 8 (2) (2019) 108–120.
- [46] S. Verma, Performance characteristics of an annular conical aerospike nozzle with freestream effect, *Journal of Propulsion and Power - Journal of Propulsion and Power* 25 (2009) 783–791.
- [47] L. Yang, X.-M. Zeng, Bézier curves and surfaces with shape parameters, *Int. J. Comput. Math.* 86 (7) (2009) 1253–1263.
- [48] S. Kim, J. Alonso, A. Jameson, A gradient accuracy study for the adjoint-based Navier-Stokes design method, in: 37th Aerospace Sciences Meeting and Exhibit, 1999.
- [49] S. Khare, U.K. Saha, Rocket nozzles: 75 years of research and development, *Sadhana - Acad. Proc. Eng. Sci.* 46 (2) (2021) 1–22.